Construction and Building Materials 473 (2025) 140873

Contents lists available at ScienceDirect

Construction and Building Materials

journal homepage: www.elsevier.com/locate/conbuildmat

The critical role of time-dependent rheology for improved quality control of 3D printed cementitious structures

Yu Jiang, Qingxin Zhang [1], Abir Al-Tabbaa, Ronan Daly *

Department of Engineering, University of Cambridge, UK

ARTICLE INFO

Keywords:
3D printing
Cementitious materials
Print quality
Time-dependence
Rheology
Filament
Mesostructure

ABSTRACT

3D printing of cementitious materials is gaining momentum as a method of construction across length scales, from patterned coatings to full-scale structures. The technology also enables cutting-edge research in hierarchical architectures and in carbon storage applications. Cement-based material printing faces challenges because colloidal flocculation and hydration reactions transition the material from a printable fluid to a solid over time. This drives continuous changes in material printability and can lead to unpredictable macroscopic properties. It is therefore critical to give manufacturers quality control metrics that will link their cement-based formulations to the macroscopic properties of the final printed products. Here, we report a first step to progress this with a small-scale cement paste extrusion printing study. We examine the cement paste rheological properties that link closely to flows experienced during printing, quantify the changes over time and show how these influence changes in extrusion pressure and filament cross-sectional morphology. We then use numerical simulations to help understand these experimentally observed changes. We observe a time when both the cement paste's static yield stress and the extrusion pressure suddenly increase, coinciding with a change in filament morphology. Importantly, this change in printing behaviour occurs at approximately half the Open Time, the conventionally defined metric for printability and we observe a 29 % reduction in the interlayer contact area between filaments, which can increase macroporosity and drive down load-bearing capacity. This allows us to define 'print quality assurance time', a metric that takes into account the dynamic nature of cementitious materials to ensure predictable mesostructures and in turn controlled macroscopic properties.

1. Introduction

3D printing has already been adopted as a rapid design-to-product translation technology in the automotive, aerospace, architectural, biomedical and food sectors [1–3]. It has now transitioned beyond temporary, geometrical and scaled-down representations of products to fully functional, large-scale or structural parts, such as turbine blades, heat exchangers and 3D-printed houses [4–7]. Tailoring mesostructures at the printed filament scale using 3D printing is a controlled route to modify the properties at the macroscopic scale [6,8,9] and realise structures with complex geometries that are unachievable or more costly when using conventional manufacturing techniques [10,11].

Over the past decade, the world has witnessed a great boom in 3D printing of cementitious materials. Numerous trial projects, for example 3D-printed houses and bridges, have been carried out worldwide [12–16]. The adoption of 3D printing in construction comes with many potential benefits, such as materials savings [17], waste minimisation [18], heightened design freedom [10], realising complex-shaped structures without a rise in cost [5], to name just a few. In December 2023, its importance was recognised with joint efforts between ISO and ASTM to create ISO/ASTM 52939:2023 [19], a guidance for the production and delivery of high-quality 3D-printed structures.

However, compared with other materials, the 3D printing of cementitious materials involves significant additional complexity because of their transient rheological behaviour from the point of mixing with water to printing and final curing. Freshly mixed cementitious materials exhibit time-dependent rheological properties stemming from colloidal flocculation (reversible thixotropy) and hydration reactions (irreversible) which cause them to age [20]. While it is known that an increase in apparent viscosity over time must result in a change in the viscous stress term of the Navier-Stokes equation (discussed later in Section 3) and that this is critical to consider when studying the

* Corresponding author.
E-mail address: rd439@cam.ac.uk (R. Daly).
[1] Now at Department of Chemical and Environmental Engineering, University of Nottingham Ningbo China

https://doi.org/10.1016/j.conbuildmat.2025.140873
Received 8 January 2025; Received in revised form 3 March 2025; Accepted 13 March 2025
Available online 31 March 2025

extrusion process, it is currently poorly understood how these alterations in rheology may drive changes in the cross-sectional morphology of extruded filaments. Any changes in filament shape will change how they pack and are bonded together and in turn change the macroscopic properties of a 3D printed structure such as macroporosity and mechanical properties (as illustrated in Fig. 1, using an agreed definition for macroporosity [21]). When we look at other studies and their terminologies, this is equivalent to studying the combined macro-pores and micro-channels reported by Moini et al. [22], also referred to as air voids elsewhere [23–26]. These changes are anticipated to dramatically change the load-bearing capacity of final printed structures [27].

The sector defined and widely adopted a printability time limit, known as Open Time to indicate the limit beyond which a cementitious material is no longer printable [16,28–35]. In recent years, many authors have recognised a systemic flow rate reduction as the printing material ages [36–38], most likely due to a range of potential hardware deficiencies, such as an inability to provide the required pressure or insufficient filling of pump cavities as the material increases in viscosity. Chen et al. [36] defined further parameters, namely the Extrudability Window and Operation Window, to ensure print quality is maintained by regulating flow rates. These two parameters are defined as the period during which the decrease in volumetric flow rate from the original value (at a pre-set pump rate) is within 5 % and 30 %, respectively. There have also been recent studies on the effects of printing parameters (mainly flow rate, nozzle speed and nozzle height) on filament morphology, which contributed to increased control over filament morphologies [39–43]. As noted, the effects of material ageing and associated time-dependent rheology have been observed to be important to flow rate and printability, but there has been no detailed analysis of their influence on the mesostructured scale and the final macroscopic print quality.

Here, we quantify and model the change in rheology with material ageing for a standard 3D printable cement paste formulation and study through small-scale extrusion experiments and numerical studies the effects of changing rheology on the extrusion process and the subsequent changes in filament cross-sectional morphology. We overcome the challenge of systemic flow rate reduction over time through experimental design and also take into account the fluctuations in instantaneous flow rate that are impossible to avoid with such printing systems. This ensures our findings can be interpreted with confidence and will give a pathway to ensuring reliable mesostructures and hence macroscopic properties. We introduce a new and more targeted quality assurance indicator based on our findings, herein referred to as the Print Quality Assurance Time (PQAT), that takes into account the dynamic nature of cementitious material printing and we demonstrate its benefits through comparison with existing quality control parameters, such as Open Time. Overall, this work firstly provides new insights to guide larger scale printing studies and secondly immediately supports studies where small scale 3D printing is still essential, for example research in architectured materials with multi-scale structural design [44,45], carbon capture and storage [46,47] and self-sensing for structural health monitoring [48].

2. Materials and methods

2.1. Raw material

A high strength Portland cement CEM-I 52.5 N (Ketton Batch 417) complying with BS EN 197–1 [49], with an apparent density of 0.9–1.5 g/cm^3 was sourced from Heidelberg Materials UK Limited. A viscosity modifying agent (VMA) based on a hydroxypropyl methylcellulose (HMPC) powder was purchased from Alfa Aesar. Sika ViscoCrete 10, a modified polycarboxylate-based superplasticiser (SP), was supplied by Sika. Tap water was used for formulating cement paste. Formulations are discussed in the next subsection.

2.2. Specimen manufacturing process

2.2.1. Printing material formulation and preparation

The rheological properties of cementitious materials greatly affect the extrusion pressure required during printing and the shape retention capability of the filament after extrusion [50,51]. Normally, a viscosity modifying agent (VMA) and a high-range water-reducer (superplasticiser, SP) are added to cement paste to tune its flow behaviours. A standard formulation selected for this study (labelled as VMA0.6SP0.5) has a water-to-cement ratio of 0.26 and the mass percentages of VMA and SP are 0.6 % and 0.5 % of cement weight, respectively. Overall, this means the mass percentage is 78.68 % cement, 20.46 % water, 0.47 % VMA, and 0.39 % SP. A Kenwood Chef Kitchen Stand mixer, with a motor power of 1000 W and nine variable speeds, was employed together with an aluminium K-beater for mixing cement paste. As the rheological properties of cementitious materials are highly sensitive to shear history and material age, the following procedures were strictly followed. The raw materials were weighed as per the mix proportion. Cement and VMA were first mixed in a dry condition for approximately 2 min at the minimum speed (beater RPM = 133.8 ± 0.6, planetary RPM = 52.5 ± 1.6). The material ages were recorded from when water contacted powder materials, and the mixture was wet-mixed at speed 1 (beater RPM = 207.3 ± 3.7, planetary RPM = 92.1 ± 1.2) for 2 min. After that, the mixer was stopped for 1.5 min to manually scrape the surfaces of the mixing bowl and vane to eliminate the sticking material. The mixture was then mixed at speed 3 (beater RPM = 284.0 ± 6.8,

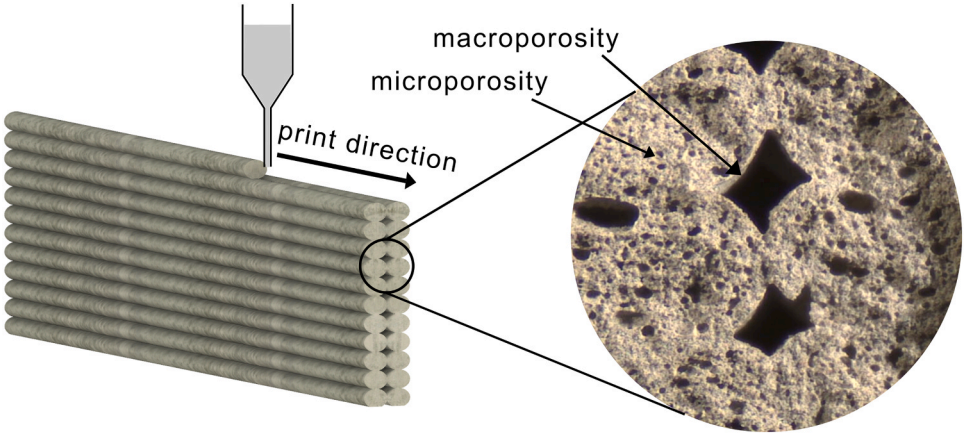

Fig. 1. Layered stacking process in 3D printing. (a) A schematic representation of the 3D printing process. (b) An image of the cross-section of a 3D printed cement paste sample, using optical microscopy and indicating macroporosity and microporosity.

planetary RPM = 125.0 ± 1.5) for another 5 min. At the time of 8.5 min after the initial water-cement contact, the mixing was stopped for manual scaping again. The mixture was then vibrated for 1 min at 30 rpm to expel entrained air.

2.2.2. 3D printing setups and parameters

A schematic of the bespoke 3D printing setup is given in Fig. 2, which is a scaled-down representation of a large-scale 3D printer, with storage of material in a reservoir, material delivery to the printhead, and finally filament extrusion and deposition onto a substrate. This system was designed to maintain a stable flow rate delivery. Similar systems were implemented in previous studies [22,45,46,52]. A compression sensor was integrated at the rear of the syringe plunger delivering the cement paste, enabling in-line monitoring of the printing pressure as it was pushed by the syringe pump.

We employed a Fisnar 5200 N gantry robot manipulator with a resolution of 0.01 mm to accurately position the printhead. Glass microscope slides (thickness tolerance ± 0.01 mm) were used as a printing substrate, and prior to printing were positioned on a double tilt and rotation stage manufactured by Comar Optics Ltd, which was levelled using Laserliner MasterLevel Box Pro with an electronic slope precision at ± 0.1°. The prepared cement paste was loaded into syringe barrels from the rear. A thin plastic tube was inserted together with the piston to release the air in the rear. A cap was installed at the tip of the syringe orifice to prevent moisture loss, both of which were then removed before the syringes were installed onto a KD Scientific Legacy KDS 410 high pressure syringe pump (accuracy of ± 1 %) to drive 3D printing. Tubing was connected to the nozzle and syringe orifice via a Luer slip.

The printing parameters in experiments are as follows: the nozzle travelling speed was set at 3.83 mm/s, the volumetric flow rate was set at 0.74 mL/min, and the nozzle height was set at 1.60 mm above the glass substrate. To maintain a constant nozzle height, the nozzle tip was cleaned using propan-2-ol wipes to eliminate residue before and after each print. The effect on filament height can be found in Appendix I, Fig. I.1. The average mass flow rates (nozzle output) were measured by the mass change of a container which was placed underneath a nozzle to collect the extrudate for 1 min, which was then converted to average volumetric flow rate by dividing by the material density. We decided to perform single-filament prints for the majority of this study because of the highly controllable printing conditions. This is in contrast to multi-layer printing, where printing onto a previously deposited and deformed substrate reduces the controllability (Appendix H, Table H.1). However, we have included results of double-layer printing in Appendix H to demonstrate findings are still applicable to multilayer printing.

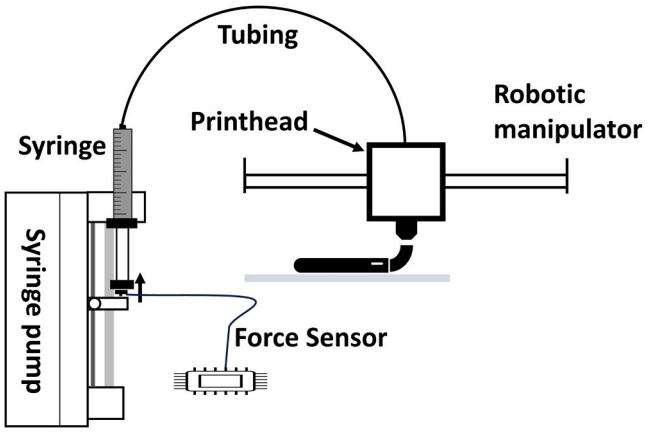

Fig. 2. A schematic representation of the bespoke 3D Printer setup.

2.3. Characterisation methods

2.3.1. Rheological properties measurement

Rheological properties were tested using an Anton Paar MCR 302 rheometer. A building material cell (BMC 90) was used for the flow curve test (Fig. B.1a in Appendix B). Parallel plates (PP-25) with a 1 mm gap were adopted for the static yield stress test (Fig. B.1b in Appendix B). The temperature was kept at 20 °C throughout the test, controlled by a Peltier base. Cement paste was carefully loaded onto the lower plate, and the excess was trimmed using a plastic spatula following the lowering of the upper plate. A solvent trap containing deionised water was employed to prevent water evaporation during the test. A pre-shear was started at 20 min post-mixing (material age) in both tests, and it lasted for 1 min. This is followed by 10 s of rest. The flow curve test started at 21 min and 10 s and then was repeated at 40, 60, 80, 100, and 120 min of material age, while the static yield stress test started at 21 min and 10 s and replicated every 22 min up to 241 min of material age. The whole flow curve development test was duplicated, while the whole static yield stress development test was repeated four times. The detailed protocols for performing the flow curve and static yield stress tests can be found in Appendix B, where the conversion factors between torque and shear stress and between speed and shear rate are also available in Appendix B, Eqs. (B.1 - B.5). The recorded ramp-down part of the shear rate versus shear stress curves (flow curves) was selected and fitted [41] using the Bingham-Papanastasiou model [53] mathematically expressed in Eq. (1). An example of model fitting can be found in Appendix B, Fig. B.1c.

$$\tau = \tau_y(1 - \exp(-m\dot{\gamma})) + \mu_p\dot{\gamma} \quad (1)$$

where τ and $\dot{\gamma}$ represent shear stress and shear rate, respectively, and τ_y represents dynamic yield stress, μ_p represents plastic viscosity, and m represents a regularisation parameter (unit: seconds). The static yield stress was determined as the peak or plateau on the shear stress versus time curve (Fig. B.1d).

2.3.2. Extrusion test

A purpose-built extruder was constructed using a high-pressure syringe pump and an integrated force sensor to measure the extrusion pressure required for all formulations while they aged. This was coupled with a mass measurement to understand changes in extrusion rate (Fig. 7c). The extrusion test was repeated at 40, 60, 80, 100, and 120 min of material age to examine the extrusion pressure development. To capture the transient extrusion behaviour of cement paste, the volumetric flow rate was set at 15.60 mL/min to finish an extrusion within 3 min, within which the rheology remains unchanged. The extrusion pressure was recorded using the integrated force sensor, and the extrusion pressure corresponding to the 20–30 mm range of piston distance was averaged and recorded as the extrusion pressure. The whole extrusion pressure development test was repeated three times.

2.3.3. Open time

Based on a previously reported method [54], the Open Time was tested by periodically printing a single line of filament, using identical printing parameters, i.e., the same pumping rate, nozzle travelling speed, and nozzle height. The Open Time is the maximum time before any discontinuity or break is observed in the printed filament, as shown in Fig. 3. This test was repeated five times.

2.3.4. Filament cross-sectional morphology

We carried out single-filament prints at different material ages until the Open Time using the printing setup and parameters prescribed in Section 2.2.2 to assess the changes in cross-sectional morphology with material ageing. These printed filaments were each cross-sectioned at multiple locations and analysed by optical microscope imaging and image analysis. The key morphological parameters of a filament cross-

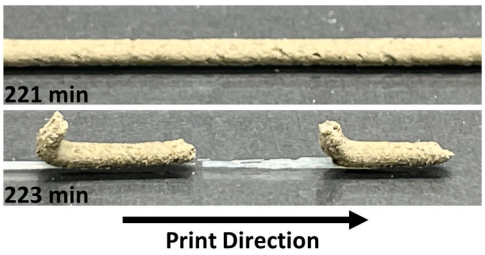

Fig. 3. Open Time test method. A consistent discontinuity occurs after continuous filaments period known as the Open Time, as shown on the lower glass surface.

section, as shown in Fig. 4, are filament width, height, and contact length with the underlying surface. The entire experiment was repeated three times.

We printed a single filament onto a glass microscope slide at designated material ages. After printing, the glass slide with the wet printed filament was quickly transferred into a confined environment for a 24-hour curing time. The filament was then detached from the substrate and continued to cure in the confined environment for another three days, prior to cross-sectioning. Only the segmented short filaments (about 45 mm long) at the middle part of the long single filament (of 75.50 mm) were attached to a sample holder and placed in a cylindrical mould with an internal diameter of 40 mm and height of 29.3 mm for epoxy resin casting. The encapsulated short filaments were fixed in a hardened epoxy resin cylinder which was then ground sequentially using 240 and 1200 SiC grit paper and then sequentially polished using 9 μm and 1 μm diamond solution to create a very flat, smooth surface finish. A specimen after processing is shown in Fig. 5. After that, the cylindrical epoxy resin sample was imaged using a ZEISS Stemi 305 optical microscope and the images were analysed using Fiji Image J [55] to extract the morphological features of the cross-sections.

2.3.5. Data normalisation

Data normalisation is needed to transform features with different ranges or units to a dimensionless form in a common scale for comparison, which can improve modelling accuracy. Data normalisation was carried out by using Eq. (2):

$$x^* = \frac{x_i - x_{\min}}{x_{\max} - x_{\min}} \tag{2}$$

where x can be different factors such as the filament width or material age in a single print, x * is the normalised value of x, x_i represents an individual measurement of x in a print, while $x_{\min}$ and $x_{\max}$ are the minimum and maximum measured values of x in this single print, respectively.

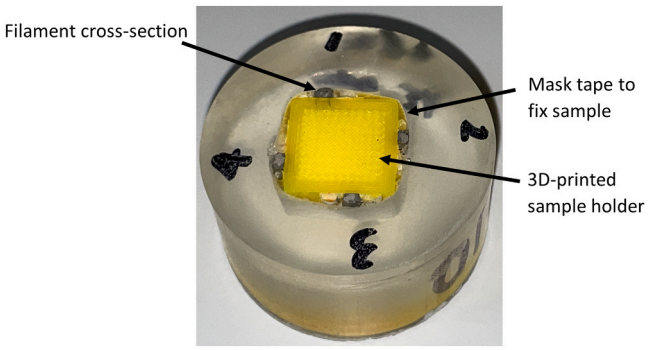

Fig. 5. A processed specimen for optical microscopic imaging. Four cementitious filaments are fixed in a hardened epoxy resin specimen with a very smooth upper surface after grinding and polishing.

3. Theory and calculation

3.1. Bingham-Papanastasiou model

The Bingham-Papanastasiou model, as shown earlier in Eq. (1), was used to fit the flow curve and obtain the key parameters - dynamic yield stress, plastic viscosity, and a regularisation parameter (m). The advantages of adopting the Bingham-Papanastasiou model are that it can fit the flow curve with high accuracy and also avoid singularity issues in the numerical simulations. The adoption of this model has recently been supported by other researchers in this field [40].

3.2. Instantaneous volumetric flow rate

As incompressibility of cement paste is assumed by many authors [39,41,42], instantaneous volumetric flow rate (Q_i) was calculated based on the measured cross-sectional area (A) as per conservation of mass, as shown in Eq. (3):

$$Q_i = Av \tag{3}$$

where v is the nozzle travelling speed, which in this case was maintained at 3.83 mm/s. Since the cross-sections were obtained from the mid-section of a strand of filament, the nozzle speed was considered constant.

3.3. Numerical modelling

There are very few prior numerical studies of the time-dependent rheology of cementitious materials and its influence of filament cross sections (as noted in Section 1 and Appendix G, Table G.1). To validate and help understand the experimental observations, a virtual printing study focusing on the deposition process was carried out. A commercial CFD software, COMSOL Multiphysics, was employed. The volume of fluid (VOF) method and the generalised Newtonian constitutive

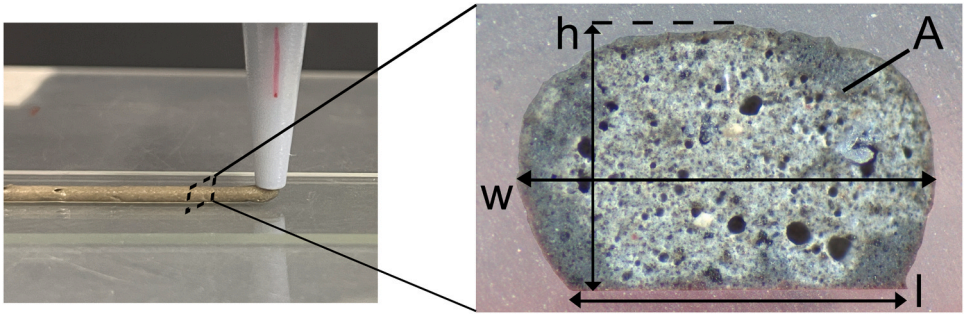

Fig. 4. Single-filament print process and filament cross-sectional features. A single filament is printed through a nozzle and deposited onto glass. Key cross-sectional features include contact length (l), filament width (w) and filament height (h), cross-sectional area (A).

relationship were adopted in the numerical modelling to trace the movement of the interface between the two immiscible fluids. The level set module (two-phase flow) and laminar flow field were coupled, given the Reynolds number of cement paste is $<<$ 1 [39]. The Bingham-Papanastasiou model (Eq. (1)) was applied as the constitutive relationship, with parameters at different material ages obtained from the experimentally measured flow curve tests noted earlier. This ensures the model takes into account the hydration and hardening processes.

The following assumptions were made: a) Cement paste is an incompressible fluid [41]; b) There is no flow at the nozzle walls [39, 41]; c) the transient rheology of cement paste is captured and remains constant during simulation time (about one min).

The governing equations of the VOF formulations on multiphase flow are shown as follows:

$$\rho\frac{\partial \boldsymbol{u}}{\partial t}+\rho(u\bullet\nabla)\boldsymbol{u}=-\nabla \mathrm{p}+\nabla\bullet\boldsymbol{\tau}+\rho\boldsymbol{g} \tag{4}$$

$$\nabla\bullet\boldsymbol{u}=0 \tag{5}$$

$$\frac{\partial\varphi}{\partial t}+\boldsymbol{u}\bullet\nabla\varphi=\gamma\nabla\bullet\left(\epsilon\nabla\varphi-\varphi(1-\varphi)\frac{\nabla\varphi}{|\nabla\varphi|}\right) \tag{6}$$

where **u** is the velocity vector field, ρ is the material density, t is time, p and **τ** represent the pressure field and stress tensor, and **g** represents the gravitational acceleration vector, φ is the volume fraction of a fluid phase, γ is the reinitialisation parameter, and ε is the interface thickness controlling parameter.

The model parameters are summarised in Table 1.

We established two models to consider two consecutive stages, firstly when filaments were extruded through the nozzle (3D model, Fig. 6a) and secondly when they were deposited on a substrate and settled into a final geometry (2D model, Fig. 6b). The 3D model was calculated for 4 s. The substrate moved at a constant velocity while the nozzle remained static as it extruded cement paste. The cross-sections of the extruded filament were taken at a distance of 6 mm from the nozzle central axis. A contour plot with cement paste volume fraction of 0.5 was determined as the boundary of a cementitious filament [56]. After that, a 2D model was established to study the settling process. This was selected due to the computational requirements of continuing with a 3D model over a long period, and because a 3D model was not required to examine this settling phenomenon. This 2D model inherited the cross-sections from the 3D model as input and retained all other parameters while cancelling out the translational velocity to create a static setting. It is worth noting that we did not take the complex rapid thixotropy recovery into account, which enhances the capacity of the filaments to resist deformation. The 2D model was calculated for another 60 s. The model geometries and boundary conditions of the 3D model and 2D model are given in Fig. 6(a, b). Numerical result validation has been carried out, including mesh refinement studies and are reported in detail in Appendix G.

Table 1
Parameter values used in numerical simulations.

Parameters	Symbols	Numerical values
Density	ρ	1.859 g/mL
Nozzle internal diameter	d	2 mm
Nozzle height	H	1.60 mm
Volumetric flow rate (input)	Q_0	0.74 mL/min
Nozzle travelling speed	v	3.833 mm/s
Surface tension coefficient	σ	Used water-air's (72.8 mN/m)
Contact angle	θ_w	0.349 rad
Dynamic viscosity	τ_y	Chosen from the measured flow curve data for the first 120 min. Extrapolated values during further increase after 120 min were also used, i.e. τ_y= 2000 Pa, μ_p= 40 Pa·s for 180 min and τ_y= 4000 Pa, μ_p= 40 Pa·s for 200 min.
Plastic viscosity	μ_p	
Regularisation parameter (m)	0.90247 s	This is fixed as the average m value during the first 120 min.
Reinitialisation parameter	γ	0.1 m/s – Chosen as just over the estimated highest velocity magnitude in the domain
Interface thickness controlling parameter	ε	Set to half of the maximum element size in the component (3D); default value (2D)

3.4. A note on scalability of results

As a fundamental study, this work directly contributes to the practical applications of structural coating and state-of-the-art research in architectured materials and CO_2 storage with cement paste, which are also all carried out at a similar small-scale of printed specimens, as illustrated earlier in Section 1. However, this work is also expected to provide a framework for quality control of large-scale 3D printing with cement mortar or concrete on a large scale, especially with 1 K systems where there is no secondary mixing step. This is because the trends of time-dependent rheology of cement mortar or concrete as they age are similar to that of cement paste which is the common matrix. Adding aggregate will change the rheology values, but it is not expected to stop apparent viscosities from increasing. Additionally, this print setup mimics the three-stage processes and components of 1 K large-scale 3D printing systems, despite being on a smaller scale. Following the same procedure outlined here, a similar trend is expected on a larger scale, which will be the subject of future manufacturing research.

4. Results and discussion

Using the techniques and theory noted in Sections 2 and 3, we will quantify the changes in rheology over time and their influence on extrusion and the printed filament morphology and then use existing models to help build our understanding and deliver an improved level of quality control.

4.1. Quantifying the change in rheological properties and effect on extrusion

Five cement paste formulations were prepared with varying concentrations of viscosity modifying agent (VMA) and superplasticiser (SP), with all details provided in Appendix A, Tables A.1 and A.2. Their rheological properties and extrusion performances were quantified and compared as they aged (Appendices C and D, Figs. C.1, C.2 and D.1c). To select a standard formulation for the investigations in the remainder of this work, a trade-off needs to be made between a low extrusion pressure (determined by low dynamic yield stress and low plastic viscosity [57]) and a good ability to hold the filament shape against deformation after extrusion during 3D printing (determined by high static yield stress [57, 58]). As a result, the formulation containing 0.6 % VMA and 0.5 % SP (VMA0.6SP0.5) was selected. This presents moderately low dynamic yield stress and plastic viscosity (Fig. 7a) with one of the highest static yield stresses of the formulations trialled (Fig. 7b), while still requiring a moderately low extrusion pressure (Fig. 7c). This formulation was used to study the effects of material ageing from 20 min to 120 min after water addition. The dynamic yield stress and plastic viscosity increased from 779.68 Pa to 997.13 Pa and from 31.65 Pa·s to 35.09 Pa·s, respectively. Meanwhile, m was slightly reduced from 1.02 to 0.87. The static yield stress showed a linear increase from 450.67 Pa to 2981.18 Pa from 21 min to 109 min, in line with the findings of other studies [59].

However, there is an inflection point close to 120 min. After that, the static yield stress development deviated from a linear increase to show an exponential increase, as validated by the excellent fitting result with R^2 of 0.999 using the Perrot exponential model [60]. The increased static yield stress (Fig. 7b) corresponds to an improved buildability [51, 61,62] and filament shape retention [50] after deposition. These changes in rheology are observed to drive the net extrusion pressure to

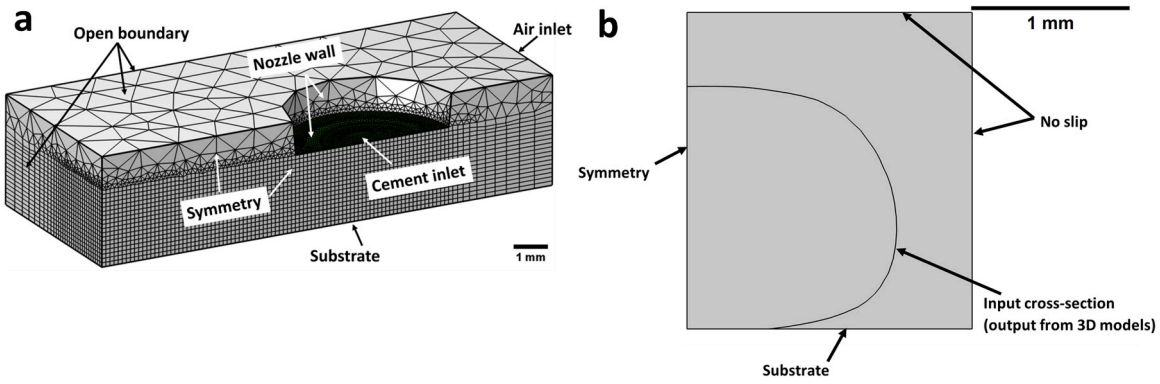

Fig. 6. Model geometries and boundary conditions: (a) 3D model; (b) 2D model.

increase from 2.13 bar at 20 min to 4.42 bar at 120 min, with a linear increase shown between 20 min and 100 min. It is noted that the slope of this pressure change increases somewhere between 100 min and 120 min, making the 120-min data deviate from the linear fit. This increase in net extrusion pressure with material ageing is shown in Fig. 7c and will clearly be important for equipment specification during scale-up and translation. Additional data from the other four formulations is given in Appendix D, Fig. D.1c, reflecting similar trends. Based on these findings, we anticipate there will be an influence on the filament cross-sectional morphology and print quality and so will examine this next to build a new level of understanding for manufacturing.

4.2. Open time determination

A consistent filament was printed with material ageing until discontinuities appeared at the determined Open Time of 221.9 ± 4.5 min. The printing pressure development during the printing process is given in Appendix D, Fig. D.2a. The systemic decrease in flow rate over time mentioned earlier in Section 1 was deliberately avoided in this study. Our designed printing system, powered by a high-accuracy syringe pump, can sustain a stable volumetric flow rate until its linear force limit (about 5.62 bar) is reached, shortly before triggering Open Time termination and the following cessation of flow. This means that for our system, the Extrudability Window and Operation Window [36] are almost identical to the Open Time and therefore are not reported further.

4.3. Effect of material ageing on filament cross-sections as a new quality assurance metric

Having examined in detail the rheological properties and their effects on the printing process, it is important for the field to further link this to mesostructures by looking at filament morphology. As noted earlier, if the filament cross-section changes with material ageing, it is anticipated to alter the mesostructures and hence macroscopic properties of a printed structure. With this in mind, we define a more targeted parameter for quality control, during which the filament cross-section remains stable. Here, we refer to it as the Print Quality Assurance Time (PQAT), and to test out this concept and define what are the changes we need to measure, we carried out highly controlled filament printing, cross-sectioning and analysis.

To examine the effects of material ageing on these parameters, three printed filaments were created at each of 12 separate times from 20 min to 220 min of material ages (i.e. to the Open Time). All the data are summarised in Appendix E, Fig. E.1. Looking at a single representative data set in Fig. 8(a, b), the filament width and height did not show any change with material ageing. However, the contact length between filament and substrate decreased significantly after 120 min (Fig. 8c). This means that during 3D printing the interlayer contact area (per unit filament length) will also decrease with material ageing. The contact length was reduced from 2.49 mm (120 min average) to 2.04 mm at 145 min (18.1 % decrease), which further decreased to 1.51 mm at 222 min (39.3 % decrease). This means that the load-bearing capacity of printed structures would be greatly reduced, because the load-bearing area would decrease at each layer. Also, this reduced contact length would drive an increase in macroporosity because of the increased spacings between filaments.

In this work, we monitored the average volumetric flow rate, as is a standard approach. This entailed recording the volume extruded over the course of a minute, which was found to remain very stable, as shown in Appendix D, Fig. D.2b. However, to look with precision at any links between flow rate and filament morphology, we needed to look at instantaneous volumetric flow rates based on filament cross-sectional area (Eq. (2)). With this approach, there is a strong correlation between the filament width and instantaneous volumetric flow rate, as shown by comparing Fig. 8a with Fig. 8d.

In light of the synchronised trend between the contact length and cross-sectional area, an adjusted contact length (l'), defined as contact length divided by cross-sectional area, is herein proposed to better reflect the effects of material ageing on contact length by offsetting the influence of instantaneous volumetric flow rates (Eq. (7)):

$$l' = l'/A \tag{7}$$

where l is contact length, and A is cross-sectional area.

As can be seen in Fig. 9a, it shows more clearly that over the first 120 min, despite fluctuating instantaneous volumetric flow rates, there was no significant change in the adjusted contact length, which indicates a stable interlayer contact area. However, a 29 % decrease in adjusted contact length can be seen when comparing the average at 120 min (0.74 mm^{-1}) to the average at 222 min (0.53 mm^{-1}), which indicates a significant decrease in interlayer contact area.

To quantify the filament cross-sectional shape, a dimensionless number (f) is herein proposed, which is defined as the ratio of the difference between filament width and contact length to the filament height, as shown in Eq. (8):

$$f = (w - l)/h \tag{8}$$

where w and h are the filament width and height, respectively, and l is the contact length. For manufacturing purposes, it is preferred to have as small a difference as possible between filament width and the contact length. This indicates that the filament cross-section is close to a rectangle with a low aspect ratio, which would drive low macroporosity and improved stability. From Fig. 9b, we can see that for the initial 120 min, the dimensionless number (f) is stable. After 120 min, there is a dramatic increase by 254.4 % at 145 min. This demonstrates that after 120 min, the shape of the filament cross-section was changed to be less flat and rectangular. We have confirmed that a near-identical trend is obtained if

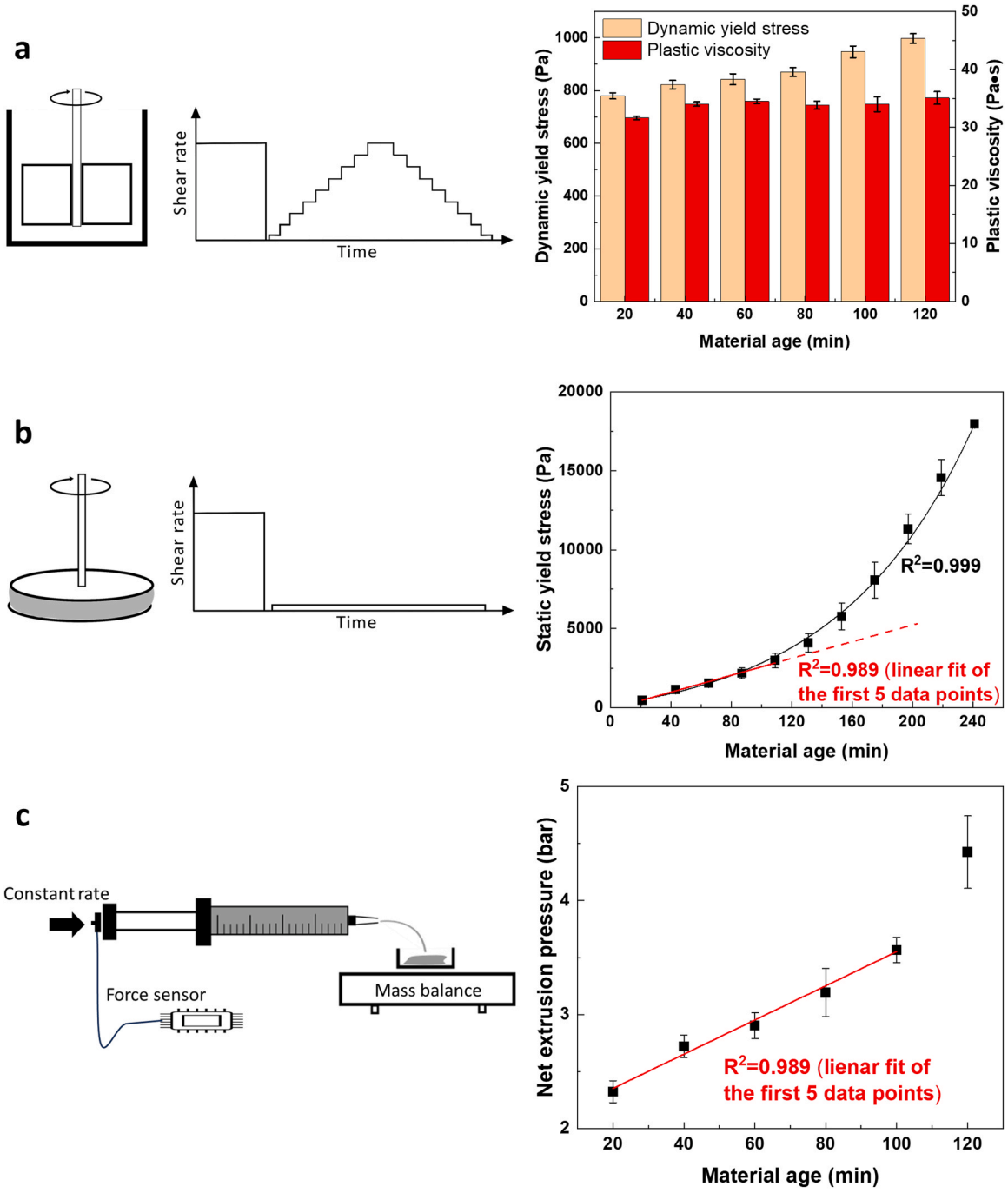

Fig. 7. Rheological properties and extrusion tests for the selected standard printing material. (a) Flow curve test setup, test protocol, and results – the development of dynamic yield stress and plastic viscosity over time. (b) Static yield stress test setup, test protocol, and results – static yield stress development over time. (c) Schematic representation of the extrusion test setup, with volumetric flow rate set at 15.60 mL/min. A linear increase can be seen up until 100 min.

we make the contact length dimensionless using $l/\sqrt{A}$. The relevance of this test was proven by showing that the interlayer contact length (i.e. filament to filament) is proportional to the contact length between filament and glass, used here as the control substrate (Appendix H, Fig. H.1). The quality assurance metric for 3D printing introduced earlier, PQAT, is therefore determined to be 120 min for this formulation. This is significantly shorter than the commonly defined Open Time. As a result, we can interpret that even while staying within the Open Time, there will be altered mesostructures after the PQAT, which will in turn compromise the macroscopic properties of the printed structures, such as increased macroporosity. The shortening of contact length (extrapolated to interlayer contact area) and change in filament cross-sectional shape due to material ageing also potentially pose a threat to load-bearing capacity which is one of the most important functionalities of 3D-printed cementitious structures. The detailed mechanical testing of printed structures is beyond the scope of this fundamental work but validation of this conclusion will be a focus of future research.

To further validate that material ageing can affect filament morphology during 3D printing, we normalised parameters using Eq. (6) and plotted the normalised filament width and normalised contact length against normalised cross-sectional area and normalised material age, respectively. The plots are provided in Appendix F, Figs. F.1b and F.1c. This confirmed that material ageing did not affect the filament width, noting that the axis of normalised filament width is parallel to the

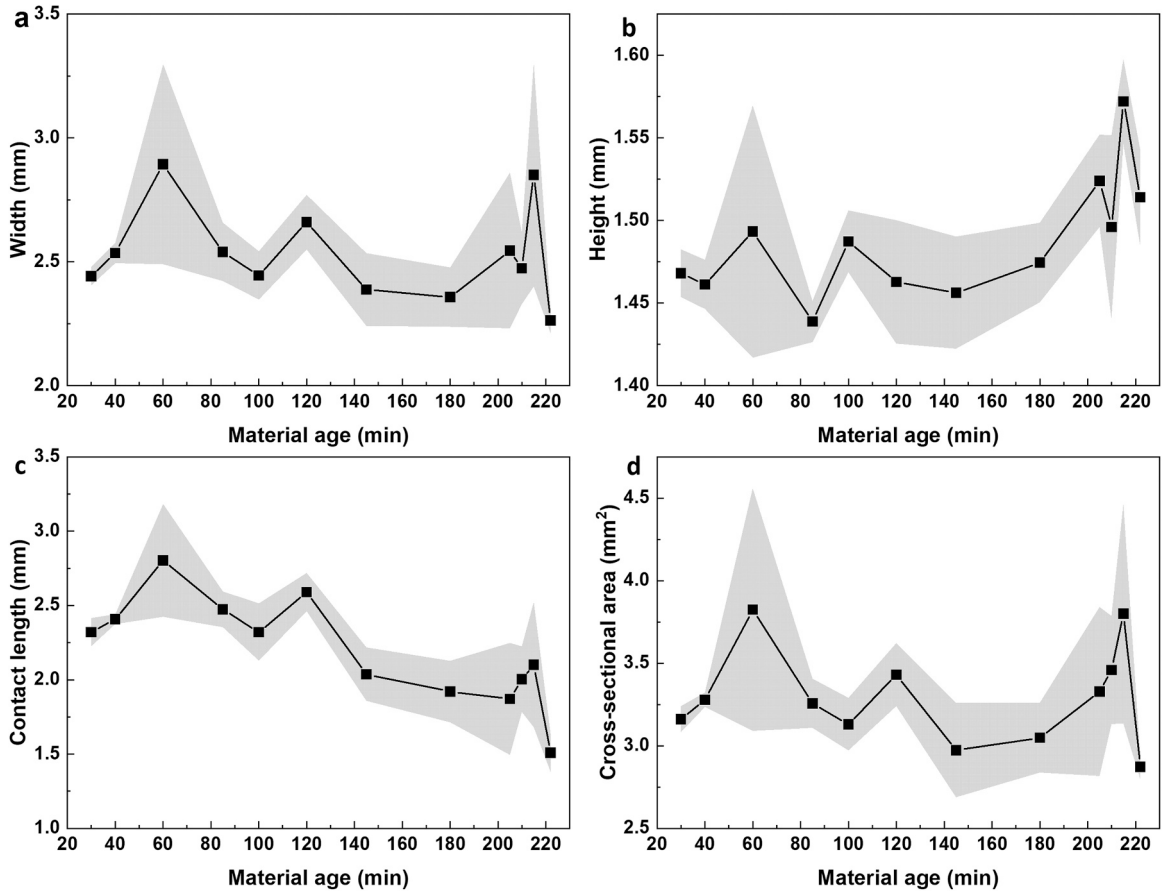

Fig. 8. Filament cross-section morphology development with material ageing. (a) Filament width remained stable, with data correlated closely to area. (b) Filament height remained stable. (c) Contact length remained stable until 120 min, then decreased. (d) Cross-sectional area remained stable, with data correlated closely with width.

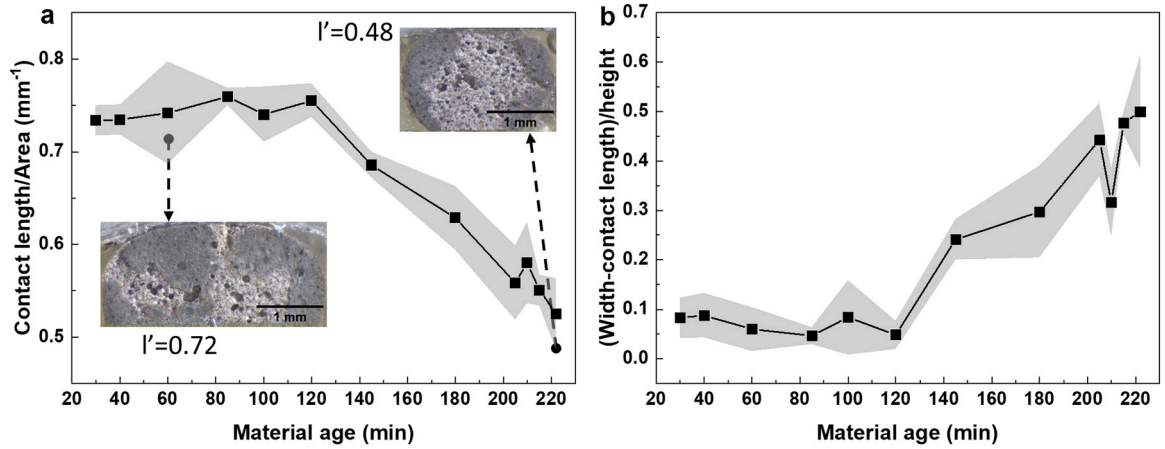

Fig. 9. Analysing cross-sectional morphology. (a) The adjusted contact length remains stable during the initial 120 min, but significantly decreases after 120 min. The cross-sectional shape moves away from the ideal to be less flat and rectangular. (b) A dimensionless number is proposed to quantify the shape of filament cross-sections and is defined as the ratio of the difference between filament width and contact length to filament height.

fitting plane. Secondly, we confirmed a positive correlation between contact length and cross-sectional area, which can be further extended to between the contact length and instantaneous volumetric flow rate if we consider a constant nozzle travelling speed, as maintained throughout all experiments. We highlight the importance of stable flow rate delivery, as with any 3D printing. Systemic changes in flow rate can lead to severe contact length decreases, as evidenced in Appendix F, Table F.3. The systemic flow rate reduction over time reported by many [36–38] therefore should be resolved to improve the state-of-the-art, potentially through hardware improvements. If flow rates remain stable, as should always be the case in 3D printing, then material ageing will be a key factor driving changes in contact length. While material ageing does not influence filament width when a stable flow rate is maintained, a systemic reduction in volumetric flow rate due to material ageing in large-scale applications, as noted earlier, will significantly affect mesostructures and increase this macroporosity further if the

filament pitch is unchanged (Appendix F, Fig. F.1a). These two issues linked to the filament morphology demonstrate why we recommend using the PQAT as a quality assurance parameter instead of only Open Time, as it guides the manufacturing to stay within parameters where filament morphology (mesostructure) remains sufficiently consistent.

4.4. Numerical verification of contact length changing with material ageing

A numerical study was carried out to identify if this would validate or help understand the experimental observations and offer a future path to improved predictability of behaviour and 3D printing control. Numerical verification of filament cross-section changes with material ageing was carried out using COMSOL Multiphysics models, as detailed in Section 3.3. An example of the deposition process is shown in Fig. 10a, with the red part representing the geometry of an extruded filament in the axisymmetric model. The predicted cross-sectional morphologies with different material ages using measured rheology data up to 120 min and extrapolated rheology data after 120 min are depicted in Fig. 10b, showing filament cross-sections almost immediately after extrusion (4 s of calculation).

We can conclude from Fig. 10b that the filament height and width remained essentially unchanged within this timeframe, showing only a 0.5 % change in filament width, 0.6 % change in filament height, and up to 7.3 % change in contact length. It is worth noting that the results obtained at a simulation time of 4 s did not reflect the final cross-section observed experimentally. When printing, it was visible to the naked eye that the filament was extruded in a shape close to a cylinder, and then it gradually settled and deformed to reach a stable contact length with the surface or layer below. This is why we see such a contrast between the simulated and experimental cross-sections shown in Fig. 10c, especially regarding contact length.

Using a 2D axisymmetric model, we calculated how the simulated cross-sections would change after settling for an additional 60 s. At this time, as anticipated from the experiments, we found a gradual increase in the contact length as the simulation progressed (settling effect), accompanied by a shortened filament width and slightly higher filament height (shown in Fig. 10d). The increase in dynamic yield stress and plastic viscosity because of material ageing represents greater resistance to deformation, which in turn leads to this change in settling. From Fig. 10d, we found that the contact lengths of 20 min and 120 min stayed similar with a negligible decrease, while a noticeable decrease was observed at 180 and 200 min. It is clear that this combination of modelling is key, with a short, computationally intensive 3D model giving excellent predictability of the filament printing over a short timeframe, and the less computationally-intensive 2D model being used to study longer timescales, the settling of the filament and the subsequent change in inter-filament contact area. It is important to note that the rapid re-flocculation (after extrusion) and solidification were not accounted for in the simulations, in line with previous studies [63]. The combined deposition model and settling model qualitatively present a decreasing trend in contact length with material ageing, which corroborates with the trend we observed in experiments, linking the changes in rheology due to material ageing to mesostructures. Details regarding model validation and mesh refinement studies can be found in Appendix G and Fig. G.1.

This is very promising and clearly reflects the experimental trends, allowing us to interpret these filament morphology changes in terms of the rheology and behaviour during settling. However, the numerical models need to be further improved to realise a more accurate prediction of the final cross-sectional morphology, especially contact length (interlayer contact area per unit length) which will be a determinant of interlayer load-bearing capacity. Future research will look at post-printing rapid re-flocculation and solidification and thixotropy recovery as a path towards improved models.

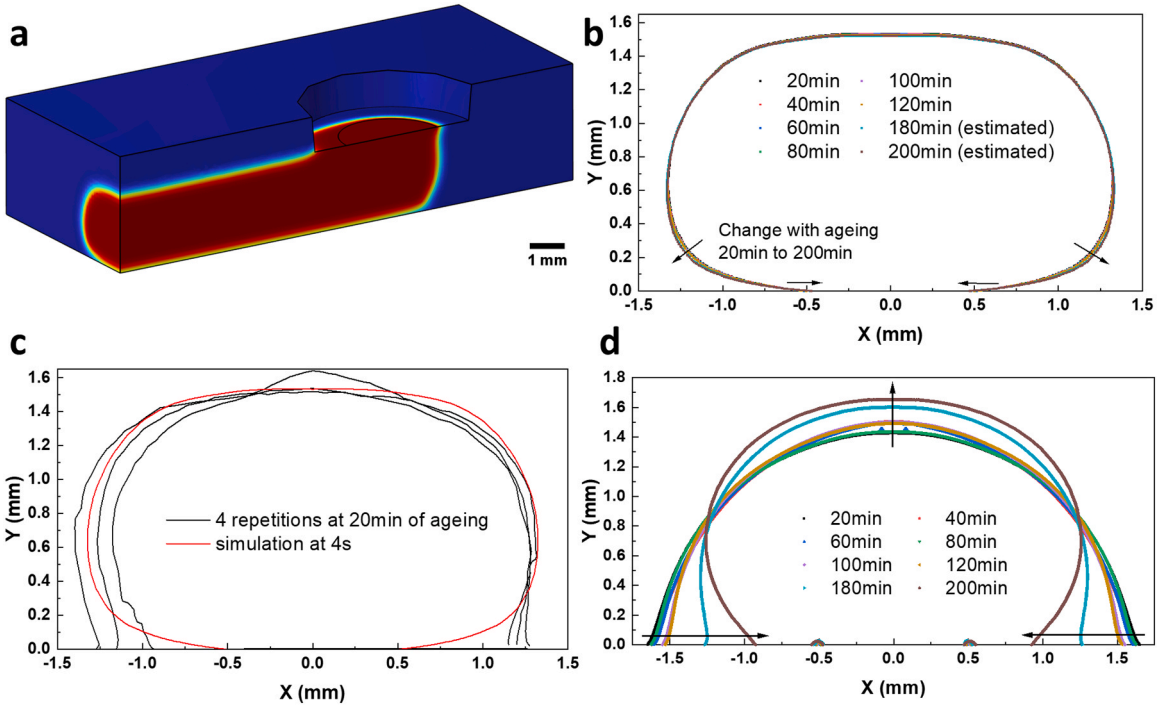

Fig. 10. Simulation results of printed filaments at different material ages. (a) 3D visualisation of the deposition process obtained at 4 s of simulation time. The colour indicates the volume fraction of cement paste, with 1 being cement paste and 0 being air. (b) Cross-sectional morphology plots for material ages at a 20-min interval from 20 to 120 min, plus two additional extrapolated data points, i.e. 180 and 200 min. (c) Comparison between simulated results and experimental results, showing a good prediction of filament width and height. (d) Comparison of cross-sections with different material ages. The initial 120-min data stays very close, while the contact lengths of 180 and 200 min show a significant reduction, confirming the observed decreasing trend of contact length with material ageing.

4.5. Relevance to 3D printing with multiple layers

To create a structure involves overlaying more than one filament, and so we performed double-layer prints. The contact length with the first-layer filament (interlayer contact length) shows the same trend as the contact length between the first-layer filament and the glass slide (filament-to-glass), as evidenced in Appendix H, Fig. H.1. This demonstrates that the PQAT can also ensure a consistent filament cross-section in multi-layer printing, when creating a full structure.

4.6. Discussion

The challenge of ageing of cementitious materials is currently addressed by quantifying and remaining within the conventionally defined Open Time. We observed a significant deviation from the desired filament morphology after only 120 min (almost half of the Open Time). With the changing rheology as the material ages, the filament width and height remaining unaffected, while the contact length steadily decreases. This means the filament cross-sectional morphology moves steadily away from an approximated rectangular shape and has an increased curvature close to the underlying layer. This automatically increases the size of the gap or voids trapped between printed filaments. The reduced interlayer contact area would also potentially impact the interlayer load-bearing capacity on a macroscopic scale, which is one of the most important functionalities of final printed cementitious structures. While analysing the data, it became clear that there were minor fluctuations in the volumetric flow rate over short timescales, evidenced by fluctuating cross-sectional areas even within one filament. By examining the contact length with respect to the cross-sectional area, it confirmed very clearly that this change in morphology was occurring. This trend was further supported by the numerical modelling. We defined a PQAT, that can ensure print quality by ensuring consistent mesostructures, which determine the macroscopic properties of the final printed products. This PQAT quality metric is expected to be a much more useful parameter to consider when 3D printing, compared with the more traditional parameter of Open Time. Rather than focusing on the ability to deliver a continuous filament, PQAT gives a more detailed predictability of the cross-sectional morphology of the filament. This leads to an improved level of control over macroporosity and dimensional accuracy, which subsequently leads to more repeatable interlayer adhesion and macroporosity as well as improved mechanical, thermal and load-bearing properties. While it is not tested in this work, this indicates that the durability of 3D-printed cements and concrete could be negatively affected after the PQAT. Water permeability and ion ingression are expected be more severe with shortened interlayer contact area and greater macroporosity [64], which may also lead to poor freeze-thaw properties. The suggested approach of the quality assurance factor linked to the actual filament morphology is demonstrated as essential when trying to keep track of mesostructures with material ageing.

3D printing relies on accurate, stable material dispensing. We highlight the importance of flow rate output which can cause filament thinning. Compared with the effects of material ageing on contact length, the influence of flow rate was proven higher. This is especially a problem in large-scale 3D printing, where there is a systemic flow rate reduction over time.

5. Conclusions

In this paper, we established a highly controllable 3D printing system with printing pressure in-line monitoring capability, which enabled us to study the effects of material ageing on mesostructures (filament morphology) with controlled printing parameters. This system eliminates the systemic flow rate decrease over time, which is essentially an effect of material ageing. Overcoming the challenges of flow rate fluctuations at an instantaneous scale, we pinpointed the fundamental alteration in filament cross-sections with material ageing, supported by CFD numerical simulations. A more targeted quality assurance parameter was therefore defined. The following conclusions can be drawn from this work as follows:

1) We quantified rheology changes, such as yield stress and plastic viscosity increases with the progress of printing time, which are referred to as material ageing. The static yield stress changed from a linear increase to an exponential increase. The transition point coincides with the PQAT. Such changes in rheology increased cementitious materials' resistance to flow and drove increased extrusion and printing pressure. The quantified time-dependent rheological parameters can be used to predict dynamic 3D printing behaviour and provide a deeper understanding of the printing process.
2) Conventional quality control parameters were unable to ensure consistent filament cross-sections. As the material aged, the shape of filament cross-sections was significantly altered after an initial stable window where a consistent cross-section can be obtained. Importantly, this change in printing behaviour occurs at approximately half the Open Time, the conventionally defined metric for printability. The filament cross-sectional shape significantly deviated from a rectangle with a low aspect ratio to become less flat and rectangular. This meant we observed a 29 % reduction in the interlayer contact area between filaments, which can increase macroporosity and drive down load-bearing capacity.
3) Material ageing influences print quality by affecting the shape of filament cross-sections and contact length. Material ageing does not cause filament thinning here, but flow rate is proportionate to filament width. In terms of contact length, flow rate is found to have a more significant influence than material ageing. This highlights that accurate, stable flow rate output is of paramount importance, but the role of material ageing in quality control should not be underestimated in 3D printing.
4) In light of such changes in filament cross-sectional morphology, we defined a new quality control parameter, print quality assurance time (PQAT), to represent the limit of that initial stable window. This parameter ensures consistent mesostructures. By applying the principles of architectured materials, the macroscopic properties of final printed products can be ensured. This study brought about a methodology for establishing quality control of 3D printing at a mesoscopic level (mesostructures).
5) The established numerical models qualitatively proved altered filament cross-sectional morphologies and decreased contact length after the PQAT. The 3D model predicted the filament width and height well. The 2D model, using the predicted filament cross-section from the 3D model as input, showed a decreasing trend in contact length during the settling process, although a quantified prediction needs further studies.
6) These conclusions are expected to be directly applicable to cement mortar or concrete if scaled up with a 1 K system, and the extrusion-based 3D printing of other materials with transient rheological properties, such as epoxy resins. For 3D printing with a 2 K system, the time-dependent rheological properties will still have a significant impact, which is worth further investigations.

In this first study, we have quantified the time-dependent rheology of cementitious materials and its effect on 3D printing behaviour. In addition, we established a PQAT metric to guide practitioners on how to preserve a constant filament cross-sectional morphology, and therefore maintain consistent mesostructures and final print quality. This will drive further growth in 3D printing of cementitious materials both in academia and in the industry by improving repeatability and consistency in the macroscopic properties characterisation of 3D printed products and we hope will support the wider market adoption of 3D printing in the construction of structures and infrastructure.

CRediT authorship contribution statement

Daly Ronan: Writing – review & editing, Validation, Supervision, Resources. **Al-Tabbaa Abir:** Writing – review & editing, Supervision. **Zhang Qingxin:** Writing – review & editing, Investigation. **Jiang Yu:** Writing – original draft, Validation, Methodology, Investigation, Formal analysis, Data curation, Conceptualization.

Declaration of Competing Interest

The authors declare that they have no known competing financial interests or personal relationships that could have appeared to influence the work reported in this paper.

Acknowledgements

The authors acknowledge studentship funding from the Cambridge Trust and CSC-Cambridge International Scholarship. The authors acknowledge the Engineering and Physical Sciences Research Council (EP/S009000/1) for support of Dr Qingxin Zhang.The authors also acknowledge Etienne Vaquier for help with experimental procedures, Heidelberg Materials UK Limited for provision of the cement used in this study, and Sika Limited for the provision of the superplasticiser used in this study. Last but not least, the authors acknowledge the valuable suggestions provided by Prof Alexandre J. Kabla and Dr Ana Blanco.

Appendix A. Supporting information

Supplementary data associated with this article can be found in the online version at doi:10.1016/j.conbuildmat.2025.140873.

Data availability

All data required to evaluate the conclusions of this study appears in the paper and/or the Appendices. Other relevant data supporting the findings of this study are available from the corresponding author upon reasonable request. Source data are provided in this paper.

References

[1] T.D. Ngo, et al., Additive manufacturing (3D printing): a review of materials, methods, applications and challenges, Compos., Part B 143 (2018) 172–196.
[2] M. Saadi, et al., Direct ink writing: a 3D printing technology for diverse materials, Adv. Mater. 34 (28) (2022) 2108855.
[3] S. Zhu, et al., Extrusion-based 3D printing of food pastes: correlating rheological properties with printing behaviour, Innov. Food Sci. Emerg. Technol. 58 (2019) 102214.
[4] A.H. Alami, et al., Additive manufacturing in the aerospace and automotive industries: recent trends and role in achieving sustainable development goals, Ain Shams Eng. J. 14 (11) (2023) 102516.
[5] D.D. Camacho, et al., Applications of additive manufacturing in the construction industry–a forward-looking review, Autom. Constr. 89 (2018) 110–119.
[6] M.A. Skylar-Scott, et al., Voxelated soft matter via multimaterial multinozzle 3D printing, Nature 575 (7782) (2019) 330–335.
[7] D. Yoo, New paradigms in hierarchical porous scaffold design for tissue engineering, Mater. Sci. Eng.: C. 33 (3) (2013) 1759–1772.
[8] R.S. Ambekar, et al., Topologically engineered 3D printed architectures with superior mechanical strength, Mater. Today 48 (2021) 72–94.
[9] J.R. Raney, J.A. Lewis, Printing mesoscale architectures, MRS Bull. 40 (11) (2015) 943–950.
[10] N. Labonnote, et al., Additive construction: state-of-the-art, challenges and opportunities, Autom. Constr. 72 (2016) 347–366.
[11] E.B. Duoss, et al., Three-dimensional printing of elastomeric, cellular architectures with negative stiffness, Adv. Funct. Mater. 24 (31) (2014) 4905–4913.
[12] F.P. Bos, et al., The realities of additively manufactured concrete structures in practice, Cem. Concr. Res 156 (2022) 106746.
[13] J. Xiao, et al., Large-scale 3D printing concrete technology: current status and future opportunities, Cem. Concr. Compos 122 (2021) 104115.
[14] G.H. Ahmed, A review of "3D concrete printing": materials and process characterization, economic considerations and environmental sustainability, J. Build. Eng. (2023) 105863.
[15] T.A. Salet, et al., Design of a 3D printed concrete bridge by testing, Virtual Phys. Prototyp. 13 (3) (2018) 222–236.
[16] R. Robayo-Salazar, et al., 3D printing with cementitious materials: challenges and opportunities for the construction sector, Autom. Constr. 146 (2023) 104693.
[17] Y. Weng, et al., Comparative economic, environmental and productivity assessment of a concrete bathroom unit fabricated through 3D printing and a precast approach, J. Clean. Prod. 261 (2020) 121245.
[18] G. De Schutter, et al., Vision of 3D printing with concrete—technical, economic and environmental potentials, Cem. Concr. Res 112 (2018) 25–36.
[19] ISO/ASTM, Additive manufacturing for construction — Qualification principles — Structural and infrastructure elements, International Organization for Standardization, Geneva, 2023.
[20] Q. Yuan, et al., Effect of mineral admixtures on the structural build-up of cement paste, Constr. Build. Mater. 160 (2018) 117–126.
[21] B. Panda, et al., The effect of material fresh properties and process parameters on buildability and interlayer adhesion of 3D printed concrete, Materials 12 (13) (2019) 2149.
[22] R. Moini, et al., Quantitative microstructural investigation of 3D-printed and cast cement pastes using micro-computed tomography and image analysis, Cem. Concr. Res 147 (2021) 106493.
[23] S. Jang, et al., Effect of material extrusion process parameters on filament geometry and inter-filament voids in as-fabricated high solids loaded polymer composites, Addit. Manuf. 47 (2021) 102313.
[24] Y.W.D. Tay, et al., Time gap effect on bond strength of 3D-printed concrete, Virtual Phys. Prototyp. 14 (1) (2019) 104–113.
[25] Y. Chen, et al., Characterization of air-void systems in 3D printed cementitious materials using optical image scanning and X-ray computed tomography, Mater. Charact. 173 (2021) 110948.
[26] J. Van Der Putten, et al., Microstructural characterization of 3D printed cementitious materials, Materials 12 (18) (2019) 2993.
[27] M.P. Serdeczny, et al., Experimental and analytical study of the polymer melt flow through the hot-end in material extrusion additive manufacturing, Addit. Manuf. 32 (2020) 100997.
[28] T.T. Le, et al., Mix design and fresh properties for high-performance printing concrete, Mater. Struct. 45 (2012) 1221–1232.
[29] C. Liu, et al., Effect of sulphoaluminate cement on fresh and hardened properties of 3D printing foamed concrete, Compos., Part B 232 (2022) 109619.
[30] P. Sukontasukkul, et al., Effect of synthetic microfiber and viscosity modifier agent on layer deformation, viscosity, and open time of cement mortar for 3D printing application, Constr. Build. Mater. 319 (2022) 126111.
[31] R.A. Buswell, et al., 3D printing using concrete extrusion: a roadmap for research, Cem. Concr. Res 112 (2018) 37–49.
[32] L. Wang, et al., Inclined 3D concrete printing: build-up prediction and early-age performance optimization, Addit. Manuf. 71 (2023) 103595.
[33] Y. Tao, et al., Twin-pipe pumping strategy for stiffening control of 3D printable concrete: from transportation to fabrication, Cem. Concr. Res 168 (2023) 107137.
[34] A.C.M. Soares, et al., Comprehensive design methodology for 3D printing mortars, Constr. Build. Mater. 401 (2023) 132804.
[35] Y. Chen, et al., Improving printability of limestone-calcined clay-based cementitious materials by using viscosity-modifying admixture, Cem. Concr. Res 132 (2020) 106040.
[36] Y. Chen, et al., 3D printing of calcined clay-limestone-based cementitious materials, Cem. Concr. Res 149 (2021) 106553.
[37] M. Li, et al., Experimental investigation of fresh and time-dependent rheological properties of 3D-printed cementitious material, Therm. Sci. Eng. Prog. 45 (2023) 102089.
[38] H. Lee, et al., Experimental study on time-dependent changes in rheological properties and flow rate of 3D concrete printing materials, Materials 14 (21) (2021) 6278.
[39] Z. Liu, et al., Modelling and parameter optimization for filament deformation in 3D cementitious material printing using support vector machine, Compos., Part B 193 (2020) 108018.
[40] G. Rizzieri, L. Ferrara, M. Cremonesi, Numerical simulation of the extrusion and layer deposition processes in 3D concrete printing with the Particle Finite Element Method, Comput. Mech. (2023) 1–19.
[41] R. Comminal, et al., Modelling of 3D concrete printing based on computational fluid dynamics, Cem. Concr. Res 138 (2020) 106256.
[42] R.J. Wolfs, T.A. Salet, N. Roussel, Filament geometry control in extrusion-based additive manufacturing of concrete: the good, the bad and the ugly, Cem. Concr. Res 150 (2021) 106615.
[43] J. Spangenberg, et al., Numerical simulation of multi-layer 3D concrete printing, RILEM Tech. Lett. 6 (2021) 119–123.
[44] S.M. Sajadi, et al., Direct ink writing of cement structures modified with nanoscale additive, Adv. Eng. Mater. 21 (8) (2019) 1801380.
[45] M. Moini, et al., Additive manufacturing and performance of architectured cement-based materials, Adv. Mater. 30 (43) (2018) 1802123.
[46] N. Ralston, S. Gupta, R. Moini, 3D-printing of architected calcium silicate binders with enhanced and in-situ carbonation, Virtual Phys. Prototyp. 19 (1) (2024) e2350768.
[47] A. Douba, P. Badjatya, S. Kawashima, Enhancing carbonation and strength of MgO cement through 3D printing, Constr. Build. Mater. 328 (2022) 126867.
[48] C. Vlachakis, et al., 3D printed temperature-sensing repairs for concrete structures, Addit. Manuf. 34 (2020) 101238.
[49] En, B., 197-1: 2011 Cement. Composition, specifications and conformity criteria for common cements. 2011. p. 7-43.
[50] Y.W.D. Tay, Y. Qian, M.J. Tan, Printability region for 3D concrete printing using slump and slump flow test, Compos., Part B 174 (2019) 106968.

[51] Y. Weng, et al., Design 3D printing cementitious materials via Fuller Thompson theory and Marson-Percy model, Constr. Build. Mater. 163 (2018) 600–610.
[52] R.M. Ghantous, et al., Drying behavior of 3D printed cementitious pastes containing cellulose nanocrystals, Cement 9 (2022) 100035.
[53] T.C. Papanastasiou, Flows of materials with yield, J. Rheol. 31 (5) (1987) 385–404.
[54] G. Ma, Z. Li, L. Wang, Printable properties of cementitious material containing copper tailings for extrusion based 3D printing, Constr. Build. Mater. 162 (2018) 613–627.
[55] J. Schindelin, et al., Fiji: an open-source platform for biological-image analysis, Nat. Methods 9 (7) (2012) 676–682.
[56] L. He, W.T. Chow, H. Li, Effects of interlayer notch and shear stress on interlayer strength of 3D printed cement paste, Addit. Manuf. 36 (2020) 101390.
[57] B. Lu, et al., Study of MgO-activated slag as a cementless material for sustainable spray-based 3D printing, J. Clean. Prod. 258 (2020) 120671.
[58] A. Perrot, D. Rangeard, A. Pierre, Structural built-up of cement-based materials used for 3D-printing extrusion techniques, Mater. Struct. 49 (2016) 1213–1220.
[59] N. Roussel, A thixotropy model for fresh fluid concretes: theory, validation and applications, Cem. Concr. Res 36 (10) (2006) 1797–1806.
[60] A. Perrot, et al., Prediction of lateral form pressure exerted by concrete at low casting rates, Mater. Struct. 48 (7) (2015) 2315–2322.
[61] B. Lu, et al., Designing spray-based 3D printable cementitious materials with fly ash cenosphere and air entraining agent, Constr. Build. Mater. 211 (2019) 1073–1084.
[62] B. Lu, et al., Study of MgO-activated slag as a cementless material for sustainable spray-based 3D printing, J. Clean. Prod. 258 (2020).
[63] A. Gosset, et al., Experimental and numerical investigation of the extrusion and deposition process of a poly (lactic acid) strand with fused deposition modeling, Polymers 12 (12) (2020) 2885.
[64] M. Nodehi, et al., Durability properties of 3D printed concrete (3DPC), 142, Autom Constr, 2022 104479.

Glossary

Material ageing: With the passage of time, freshly mixed cementitious materials transition from a low-viscosity fluid to a high-viscosity solids
Material age(s): The duration after the water-cement contact
Transient rheology: Another way of referring to time-dependent rheology
Nozzle height: The distance between the nozzle tip and the upper surface of the substrate. Also known as nozzle standoff distance
Nozzle travelling speed: The speed of nozzle while it is extruding printing material onto a substrate
Filament: The cement paste strand extruded from a nozzle and deposited onto a substrate
Contact length: The length of contact between a filament and its substrate, obtained from the cross-section
Filament width: The width of a filament obtained from the cross-section
Filament height: The height of a filament obtained from the cross-section
Mesostructures: Comprising the packing of 3D-printed filaments
Macrostructures: 3D-printed products which demonstrate many macroscopic properties, including electrical, mechanical, thermal, acoustic properties
Macroporosity: The voids between filaments
Interlayer load-bearing capacity: Also known as interlayer adhesion, referring to the load-bearing capacity when the interface is subject to loading
Open time: The window within which a strand of filament can be printed onto a planar substrate without discontinuities
Print quality assurance time (PQAT): The window within which the cross-sectional morphology of printed filaments stays unchanged